PHYSICAL REVIEW MATERIALS **2**, 045602 (2018)

Role of cell deformability in the two-dimensional melting of biological tissues

Yan-Wei Li[1] and Massimo Pica Ciamarra[1,2,*]
[1]*Division of Physics and Applied Physics, School of Physical and Mathematical Sciences,*
Nanyang Technological University, Singapore 637371, Singapore
[2]*CNR–SPIN, Dipartimento di Scienze Fisiche, Università di Napoli Federico II, I-80126, Napoli, Italy*

(Received 12 January 2018; published 5 April 2018)

The size and shape of a large variety of polymeric particles, including biological cells, star polymers, dendrimes, and microgels, depend on the applied stresses as the particles are extremely soft. In high-density suspensions these particles deform as stressed by their neighbors, which implies that the interparticle interaction becomes of many-body type. Investigating a two-dimensional model of cell tissue, where the single particle shear modulus is related to the cell adhesion strength, here we show that the particle deformability affects the melting scenario. On increasing the temperature, stiff particles undergo a first-order solid/liquid transition, while soft ones undergo a continuous solid/hexatic transition followed by a discontinuous hexatic/liquid transition. At zero temperature the melting transition driven by the decrease of the adhesion strength occurs through two continuous transitions as in the Kosterlitz, Thouless, Halperin, Nelson, and Young scenario. Thus, there is a range of adhesion strength values where the hexatic phase is stable at zero temperature, which suggests that the intermediate phase of the epithelial-to-mesenchymal transition could be hexatic type.

DOI: 10.1103/PhysRevMaterials.2.045602

I. INTRODUCTION

Kosterlitz, Thouless, Halperin, Nelson, and Young (KTHNY) [1–5] suggested the melting transition in two dimensions to occur through a continuous solid-hexatic transition and a subsequent continuous hexatic-liquid transition induced by topological defects: the dissociation of bound dislocation pairs into free dislocations drives the solid into the hexatic phase, while the unbinding of dislocations into isolated disclinations drives the hexatic to liquid transition. Different melting scenarios are however possible [6–8]. In molecular systems the melting scenario depends on specific system details, as the softness and the range of pair potential [9–11], density [12], energy dissipation [13], shape and symmetry of particles [14], and so on [15–21]. In the prototypical hard disks system melting occurs through a continuous solid-hexatic transition and a subsequent first-order hexatic-liquid transition [22,23], while in systems of hard regular polygons different melting scenarios can be observed by tuning the number of edges [14]. While the melting of many systems of particles interacting via two-body potentials has been investigated, nothing is known which concerns the features of the two-dimensional melting transition of extended and deformable polymeric particles, whose shape and volume is not fixed but rather determined by the balance between the particle mechanical stiffness and the applied stresses. Particles with these feature are rather common, and include biological cells or polymeric particles such as star polymers [24,25], dendrimers [26], microgels [27], polyelectrolyte stars [28], and soft granular particles [29,30].

Here we investigate how the deformability of the particles affects the two-dimensional melting transition in the Voronoi model of epithelial cell tissues [31–35]. Indeed, the melting transition of cell tissues, which occurs in processes involving the movement of cells such as embryogenesis, tumor spreading, and wound healing [36], is of particular interest due to the recent observation of an intermediate stage in the epithelial (solidlike)-to-mesenchymal (liquidlike) transition [37–39]. The Voronoi description of cell tissues is based on an energy functional which has been derived taking into account the cell incompressibility and the monolayer's resistance to high fluctuations, as well as the contractivity of the subcellular cortex and the membrane tension due to cell-cell adhesion and cortical tension [31–35,40]. These two contributions respectively lead to a quadratic dependence of the elastic energy of a cell E on its area A and on its perimeter P, so that $E = K_A(A - A_0)^2 + K_P(P - P_0)^2$. Here A_0 and P_0 are preferred values of the cell area and of the cell perimeter, and K_A and K_P are perimeter elastic constants. In units of $K_A A_0^2$, the energy of the system is

$$e(\{\vec{r}_i\}) = \sum_{i=1}^{N}[(a_i - 1)^2 + r^{-1}(p_i - p_0)^2], \qquad (1)$$

where the sum runs over all N cells, $a_i = A_i/A_0$, and $p_i = P_i/\sqrt{A_0}$. The energy depends on two parameters, the inverse perimeter modulus $r = K_A A_0/K_P$, we fix to $r = 1$ if not otherwise stated, and the target shape index $p_0 = P_0/\sqrt{A_0}$, we will vary. To investigate Eq. (1) one needs to determine the area and the perimeter of each cell. In the Voronoi model [31–35,40] this is done performing a Voronoi tessellation of the system, and assuming each cell to have the shape of the Voronoi cell associated with its center of mass. Thus, in this model the centers of mass of the particles are the degrees of freedom of the system.

Investigating the transition as a function of p_0 is of interest as its increase biologically corresponds to a decrease of the cell-cell adhesion strength. From a physical viewpoint, p_0 plays two

---

[*] massimo@ntu.edu.sg

important roles. On the one side, it fixes the preferred shape of the Voronoi cells. For instance, for regular hexagons and regular pentagons $p_0^{\rm hex} \simeq 3.72$ and $p_0^{\rm pent} \simeq 3.81$, respectively. More generally, the increase of p_0 favors less compact shapes, and thus a reduction in the number of sides of the Voronoi cells. On the other hand, p_0 also influences the single particle shear modulus, which in the affine approximation decreases linearly with p_0, $\mu = \mu_0 r^{-1}(p_0^* - p_0)$ (see [41]), due to the quadratic dependence of the energy on p_0. μ_0 and p_0^* are constants depending on the shape of the particle. Thus, larger values of p_0 correspond to softer particles. We remark that this definition of softness concerns the shear modulus of a single macroscopic particle; it is thus different from the softness investigated in atomistic models, e.g., Ref. [9], where softness measures the contact stiffness of two-body interaction potentials.

Our results show that the value of p_0 affects the melting scenario, as on heating melting occurs via a first-order transition, at small p_0 values, or via a continuous solid-hexatic and a subsequent discontinuous hexatic-liquid transition, at larger p_0 values. To connect to the epithelial-to-mesenchymal transition of cell tissues [37–39], for which thermal motion is negligible, we have also investigated the p_0 dependence of the zero temperature stable state of the system, and found that the increase of p_0 drives a continuous solid-hexatic transition and a subsequent continuous hexatic-liquid transition, as in the KTHNY scenario. This result suggests that the hexatic phase could be of unexpected biological relevance.

II. METHODS

A. Numerical simulations

We have performed extensive molecular dynamics simulations of systems of N particles, placed in a rectangular box with aspect ratio $L_1 : L_2 = 2 : \sqrt{3}$ and area N, under periodic boundary conditions. We employ an in-house massive parallel program to tackle the high computational cost associated with the need of performing $O(N)$ Voronoi tessellations at each integration step, to evaluate the forces acting on the particles. The results presented in the main text, if not otherwise mentioned, refer to $N = 8100$, but we have considered other values of N (up to 16 384 for finite temperature and up to 102 400 for zero temperature) to show that finite-size effects are negligible. We have investigated the melting transition in the NVT ensemble, integrating the equations of motion via the Verlet algorithm, and fixing the temperature using a Langevin thermostat [42]. The initial state is prepared relaxing at fixed temperature configurations prepared by heating/cooling the system. We check for the convergence of the heating/cooling curves (see Fig. S6 [41]), an indication of the proper thermalization of the system. Energy minimization have been carried out using the conjugate-gradient algorithm as implemented in the GNU scientific library [43]. Voronoi tessellations are computed using the Boost C++ Voronoi library [44]. We remark that the high precision and numerical stability of this library resulted instrumentally to correctly minimize the energy of the system, in particular at high p_0 values where the Voronoi tessellations develop degenerate vertexes.

B. Identification of the different phases

The solid, hexatic, and liquid phases have different spatial symmetries one could reveal investigating the correlation functions of the translational and of the rotational order parameters. The positional or translational order parameter is $\psi_T(\vec{r}_j) = e^{i\vec{G}\cdot\vec{r}_j}$, where $\vec{G}$ is the first peak reciprocal lattice vector of the triangular crystal, and $\vec{r}_j$ is the position of particle j. The rotational or bond-orientational order parameter is $\psi_6(\vec{r}_j) = \frac{1}{n}\sum_{m=1}^{n} \exp(i6\theta_m^j)$, n being the number of nearest neighbors of particle j and θ_m^j being the angle between $(\vec{r}_m - \vec{r}_j)$ and a fixed arbitrary axis. In the liquid phase, both the translational and the bond-orientational order are short ranged, while in the solid phase both of them are extended, although there is no long-range translational order in two dimensions [45]. In the intermediate hexatic phase, if any, the translational order is short ranged, while the bond-orientational one is quasi-long-ranged. The bond-orientational correlation function is calculated as $g_6(r) = \langle \psi_6(\vec{r}_i)\psi_6^*(\vec{r}_j)\rangle$ with $r = |\vec{r}_i - \vec{r}_j|$. The translational correlation function is calculated as the cut of the two-dimensional pair correlation function $g(\Delta x, \Delta y)$ along the direction $(\Delta x, 0)$ of global orientation of the bond-orientational order parameter [22], so that the averaging over different configurations is possible. Another sensitive characterization [46] of the ordering properties is provided by the size scaling analysis of the order parameters averaged over regions of linear size l_b, $\Psi_T(l_b) = \frac{1}{N_{l_b}}\sum_{j=1}^{N_{l_b}} \psi_T(\vec{r}_j)$ and $\Psi_6(l_b) = \frac{1}{N_{l_b}}\sum_{j=1}^{N_{l_b}} \psi_6(\vec{r}_j)$, where N_{l_b} is the number of particles in the considered region. Indeed, according to KTHNY $\Psi_T^2(l_b)/\Psi_T^2(l) = (l_b/l)^{-x}$ and $\Psi_6^2(l_b)/\Psi_6^2(l) = (l_b/l)^{-y}$, with $x < 1/3$ and $y < 1/4$ in the solid phase, $x > 1/3$ and $y < 1/4$ in the hexatic phase, and $x > 1/3$ and $y > 1/4$ in the liquid phase. This analysis does not distinguish the coexistence region from the liquid phase, we discriminate investigating the equation of state.

III. RESULTS

A. Finite temperature

Figures 1(a) and 1(b) illustrate the temperature dependence of the exponents x and y resulting from the subblock scaling analysis (see Sec. II and Fig. S2 [41]) of the translational and of the bond-orientational order parameters, for two values of the target shape index. The values of these exponents allow us to identify the different phases, as we discussed in Sec. II. Specifically, Fig. 1(a) shows that for $p_0 = 3.0$ the melting transition occurs at $T = 0.12$ without hexatic phase. Conversely, Fig. 1(b) shows that for $p_0 = 3.5$ there is a temperature range $T = 0.054$–0.056 of apparent hexatic order. This result is consistent with the direct investigation of the translational correlation function $g(\Delta x, 0)$ and of the correlation function of the bond-orientational order parameter $g_6(r)$. Indeed, we observe that in the hexatic phase $g(\Delta x, 0)$ decays exponentially, while the bond-orientational order is quasi-long-range. In the solid state, $g(\Delta x, 0)$ decays algebraically with an exponent $-1/3$, and $g_6(r)$ shows almost no decay, following the KTHNY theory. The temperature at which $g_6(r) \sim r^{-1/4}$ is consistent with the solid-liquid transition temperature, for $p_0 = 3.0$, and with the hexatic-liquid transition temperature, for $p_0 = 3.5$.

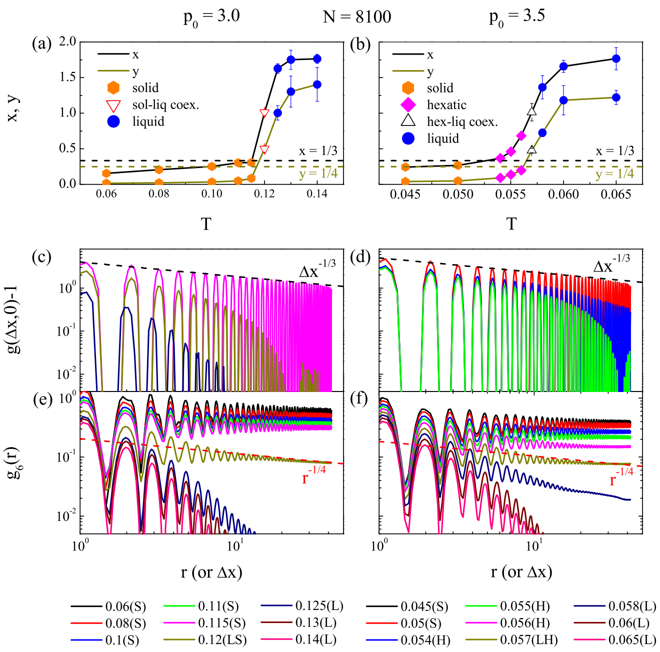

FIG. 1. Temperature dependence of the exponents x and y of the subblock analysis of the translational and bond-orientational order parameters (see text), translational correlation function $g(\Delta x,0)$, and bond-orientational correlation function $g_6(r)$, for $p_0 = 3.0$ [(a), (c), and (e)] and $p_0 = 3.5$ [(b), (d), and (f)]. The values of the scaling exponents, the decays of $g(\Delta x,0)$ and of $g_6(r)$, and the investigation of the equation of state (Fig. 2) allow us to unambiguously identify the different phases. Depending on the temperature and on p_0, states are identified as solid (S), hexatic (H), liquid-solid coexistence (LS), liquid-hexatic coexistence (LH), and liquid (L), as summarized in the bottom legend.

We have evaluated the translational length scale in hexatic and in liquid phases, and the bond-orientational length scale in the liquid phase, by fitting the corresponding correlation functions with an exponential decay $e^{-r/\xi}$. The largest length scale we measured is ∼20 (see Fig. S9 [41]), a small fraction of the box size (L_2∼84), which indicates that the finite size effects may not be strong, possibly because of the soft nature of the system [47]. We further support the absence of finite-size effects in Fig. S7 [41], where we compare the subblock plots and the two correlation functions for $p_0 = 3.0$ and $p_0 = 3.5$ for the $N = 8100$ system, illustrated in Fig. 1, with those obtained for a $N = 16\,384$ system.

Since the translational and the bond-orientational order are lost at the same temperature in the absence of the hexatic phase, and at different temperatures when this phase is present, we consistently observe in Fig. S1 [41] the associated susceptibilities to peak at the same or at different temperatures. In Fig. S5 [41] we also show that the phase identification from the subblock analysis are not affected by the thermally induced shift of the position of the first peak of the lattice, as this shift is small with respect to the width of the peak (see Fig. S4 [41]). A similar result has been observed in hard polygons [14], while the shift is relevant in systems of hard disks [22].

We identify the coexistence region investigating the equation of state, which we have determined computing the pressure via perturbation techniques [48,49], due to the many-body nature of the interaction. Figure 2 illustrates the pressure dependence on p_0, for two values of the temperature. We first notice that the pressure is negative, which indicates that the system is under tension. This is in agreement with our daily experience, as we know that the two margins of a skin cut separate. However, this is an unusual feature as systems with negative pressure are generally unstable towards the formation of cavities. The Voronoi and related models are however stable at negative pressure as the formation of cavities is hindered as particles are forced to tessellate the space. The equation of state shown in Fig. 2 illustrates the presence of Mayer-Wood loops [50], which characterize first-order phase transitions [51]. Given the phases observed on the two sides of the coexistence curve (see also Fig. S3 [41]), we understand that at $T = 0.12$ the liquid and solid phases coexist at $p_0 \approx 3.0$, while at $T = 0.05$ the liquid and the hexatic phase coexist at $p_0 \approx 3.55$. On the other hand, there is no pressure loop at the solid-hexatic transition for $T = 0.05$, which is therefore continuous.

As an additional check of the identified phases we have also visualized the system by coloring each cell according to its properties. For instance, the bond-orientational ordering is visualized by associating with each particle i a color related to the angle α between the local $\psi_6(\vec{r}_i)$ and the global Ψ_6 order parameters. Examples are in the insets of Fig. 2(b), which shows that the identified phases are consistent with their real space observation. The phase coexistence is also visualized by investigating the spatial distribution of other quantities, such as the average local perimeter-to-area ratio $\overline{\Omega}$, the average local

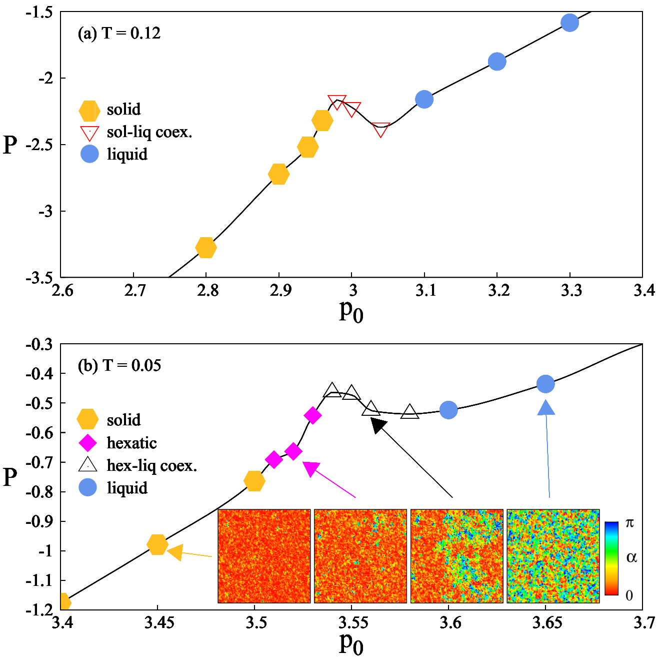

FIG. 2. p_0 dependence of the pressure at (a) $T = 0.12$ and (b) $T = 0.05$. Different symbols identify different phases, as in the legends. Lines are to guide the eye. For $T = 0.05$, snapshots of the system in the different phases are in the insets of (b). Each cell i is colored [12,22] according to the angle α between its bond-orientational order parameter $\psi_6(\vec{r}_i)$ and the global bond-orientational order parameter $\Psi_6 = \frac{1}{N}\sum_{i=1}^{N}\psi_6(\vec{r}_i)$.

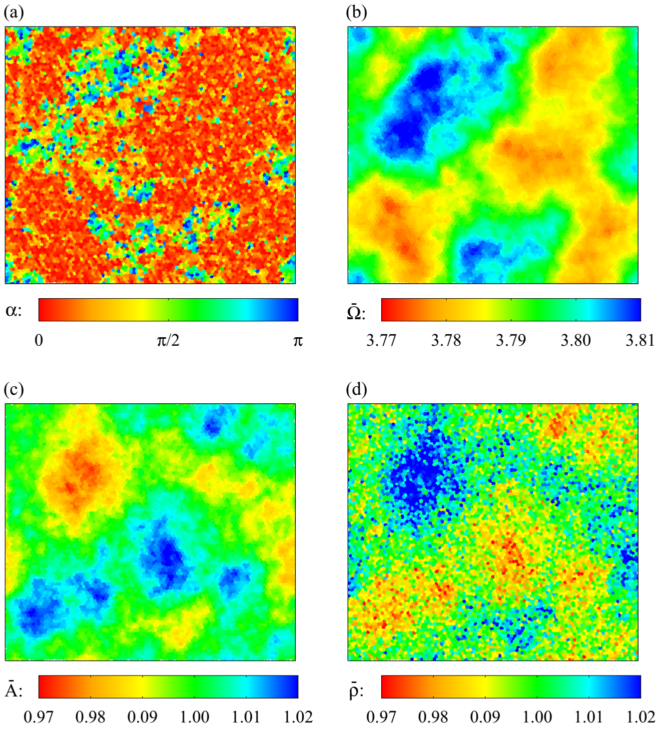

FIG. 3. Liquid-solid coexistence at $T = 0.12$ and $p_0 = 3.0$. The coexistence is seen by coloring the particles according to (a) the angle α between $\psi_6(\vec{r}_i)$ and Ψ_6, (b) the local perimeter-to-area ratio, (c) the local area, and (d) the local number density.

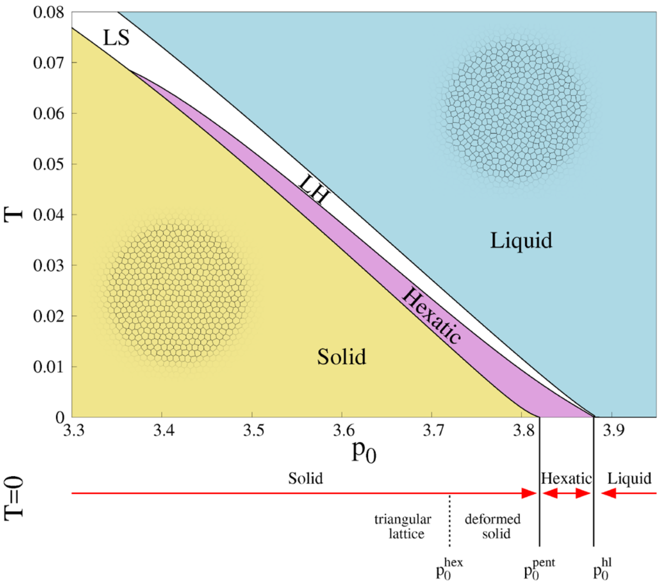

FIG. 4. Phase diagram as a function of temperature T and target shape index p_0. The lines interpolate the estimated boundaries between the different phases. The lowest temperature at which we are able to equilibrate the system depends on p_0, and varies from $T \simeq 10^{-2}$ at small p_0 values, to $T \simeq 10^{-4}$ at large p_0 values. The bottom part of the figure illustrates the properties of the zero temperature stable state as a function of p_0. The insets illustrate typical configurations in the two phases.

area $\overline{A}$, and the average local number density $\overline{\rho}$. Here we define these quantities by averaging over a circular region of radius $r_c = 10$ [14]. Interestingly, cells exhibiting solidlike behavior [red-colored regions in Fig. 3(a)] have low perimeter-to-area ratio [Fig. 3(b)], high local area [Fig. 3(c)], and low number density [Fig. 3(d)]. That is, the solid is less dense than the liquid. This unusual feature also occurs in liquids with density anomalies, such as water, and in systems with a reentrant melting transition [52].

The upper part of Fig. 4 illustrates the melting phase diagram resulting from this investigation. At small p_0 values the system melts through a first-order transition, while a two-step melting with a continuous solid-hexatic and a consecutive first-order hexatic-liquid transition appears for $p_0 \gtrsim 3.4$. While the identification of this crossover value of p_0 is difficult, we have carefully verified the absence of the hexatic phase at small p_0 values by checking the phases observed at the boundaries of the coexistence curve, which we determine through a Maxwell construction (see Fig. S8). The absence of a hexatic phase is also consistent with the fact that susceptibilities associated with the positional order and to the bond-orientational peak at the same temperature at small values of p_0 [see Figs. S1(b), S1(d), and S1(f)]. The lowest temperature at which we were able to equilibrate the system in the hexatic phase is $T = 0.0002$, at $p_0 = 3.84$. Extrapolating the solid/hexatic transition line to zero temperature we find the two-step melting scenario to extend up to $p_0 \simeq p_0^{\rm pent}$. For $p_0^{\rm pent} \leqslant p_0 < p_0^{\rm hl}$ the zero temperature state appears to be of hexatic type, and we therefore only observe a first-order hexatic-liquid transition. Due to the narrowing of the coexistence region, we do not exclude the presence of a continuous hexatic-liquid transition at p_0 values very close to $p_0^{\rm hl}$.

B. Zero temperature

The phase diagram of Fig. 4 suggests the existence of a range of p_0 values where the hexatic state is the stable state at zero temperature. This is an interesting result, as so far the hexatic phase has only been observed at finite temperature. In addition, this suggests that cell tissues, which are not thermal systems, might actually have a stable hexatic phase. We further investigate this matter evaluating the properties of zero-temperature configurations generated by minimizing the energy of the system using the conjugate gradient protocol (see Sec. II). As in the thermal case, we identify the phase of these configurations performing the subblock scaling analysis (see Sec. II) of the order parameters. We have considered minimization starting from different initial conditions: perfect hexagonal lattice, deformed solid, hexatic, liquid, random configuration, and square lattice. Here by a deformed solid we indicate a configuration with the symmetries of the hexagonal lattice, in which the cells are not perfect hexagons, alike a finite temperature hexagonal lattice configuration [see Fig. 6(a)]. The minimization terminates when the average energy per cell changes by less than 10^{-7} between consecutive minimization steps, which is our criterion for convergence, or after 10^4 steps. When the initial state is of deformed solid type, the minimization algorithm converges if p_0 is not in the $[p_0^{\rm hex}, p_0^{\rm pent}]$ range corresponding to the deformed solid configuration. We remark, however, that even when convergence is not achieved

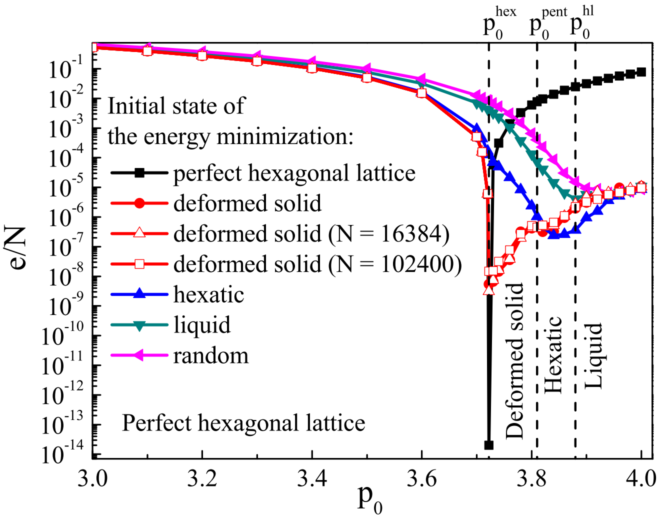

FIG. 5. p_0 dependence of the average energy per cell after performing the energy minimization algorithm. Different curves refer to minimization carried out starting from initial states with different symmetries and system sizes, as in the legend.

the geometrical features of the system appear to be clear as particles move by minute distances. However, this may not be the case for the mechanical properties of the model [53].

We show in Fig. 5 the p_0 dependence of the average energy per cell of the final state reached by our minimization procedure. The energy curve obtained minimizing the energy of the perfect hexagonal lattice has a nonmonotonic dependence, as it vanishes at $p_0 = p_0^{\mathrm{hex}}$. For smaller values of p_0, the zero temperature stable state is the hexagonal lattice, which is the final state reached when minimizing the energy starting from hexagonal, deformed solid, or hexatic configurations (e.g., see Fig. 6). We also observe that the deformed solid has the lowest energy in the p_0 range $p_0^{\mathrm{hex}} < p_0 < p_0^{\mathrm{pent}}$, while the hexatic has the lowest energy in the p_0 range $p_0^{\mathrm{pent}} < p_0 < p_0^{\mathrm{hl}} \simeq 3.88$. Both the deformed solid and hexatic configurations transform into liquidlike configurations if the energy is minimized with $p_0 \geqslant p_0^{\mathrm{hl}}$. For this large value of p_0, all of the energy curves converge except for the one obtained from the perfect hexagonal lattice, clearly indicating that the stable state is in the liquid phase and that the hexagonal phase is metastable. We notice that in the vertex model, where the tesselation is not forced to be of Voronoi type, the transition from a perfect hexagonal lattice to a disordered soft lattice at $p_0 = p_0^{\mathrm{hex}}$ has also been previously rationalized [32]. We also remark that at $p_0 = 4$ the energy of the system vanishes for a square lattice configuration. We have checked that energy minimizations starting from perfect or slightly distorted square lattices do not lead to states with energy smaller than the one we obtain minimizing the energy starting from a deformed solid configuration, unless p_0 is very close to 4 (approximately, $|p_0 - 4| < 0.05$). Thus, there is a small p_0 interval around $p_0 = 4$ where the zero temperature stable phase has the square symmetry.

The vertical dashed lines in Fig. 5 summarize the emerging zero-temperature phase diagram. We also illustrate this zero-temperature diagram in the lower part of Fig. 4, to stress that this is consistent with the zero temperature extrapolation of the finite temperature phase diagram. While the location of the different phase boundaries might be protocol dependent, the results appear to be robust as the system is able to change phase during the minimization. Specifically, we observe the following transitions in the relevant p_0 ranges during the minimization process: hexatic → deformed solid; deformed solid → hexatic; deformed solid and hexatic → liquid; deformed solid and hexatic → perfect hexagonal lattice (see Fig. 6). In Figs. 5 and 7 we also reports results obtained for a larger system size, to stress that these zero temperature results do not suffer from finite-size effects.

At zero temperature, we have found no evidence of phase coexistence, indicating that the melting transition driven by an increase of p_0 occurs through two consecutive continuous transitions, as in the prototypical KTHNY scenario. According to this scenario, the two transitions are mediated by topological defects, the solid-hexatic transition corresponding to the dissociation of bound dislocation pairs into free dislocations, and the hexatic-liquid corresponding to the unbinding of dislocations into isolated disclinations. We confirm this topological interpretation in Fig. 6 which illustrates the defects characterizing the different phases. In the perfect hexagonal lattice, there are no defects. In the deformed solid phase, defects are mainly bounded dislocation pairs (5-7-5-7 quartets). In the hexatic phase, there are isolated dislocation (5-7 pairs) and no isolated disinclination (fivefold or sevenfold defects). Finally, in the liquid phases defects are both isolated disclinations and isolated dislocations.

We have validated this topological interpretation investigating the p_0 dependence of the fraction ρ of dislocations (both isolated and clustered) and of the fraction of disclinations of the local energy minima generated from deformed solid configurations. Figure 7 illustrates the results that do not depend on the system size. As expected, we find no defects in the perfect hexagonal lattice. The fraction of cells in dislocations starts increasing at $p_0 \simeq p_0^{\mathrm{pent}}$, above which the zero temperature phase changes from deformed solid to hexatic. For $p_0^{\mathrm{pent}} < p_0 < p_0^{\mathrm{hl}}$, where the zero temperature phase is hexatic, the fraction of particles in dislocations sensibly grows, while the fraction of particles in disclinations remains low. At $p_0 > p_0^{\mathrm{hl}}$, where the system enters the liquid phase, both the fraction of cells in dislocations and that in disclinations grow.

We have also investigated the zero-temperature phase diagram for a different value of the inverse perimeter modulus $r = 100$, and found it at most weakly dependent on r. An analogous result has been reported in the investigation of the vertex model [33], where p_0^{pent} marks the location of a rigidity transition regardless of the value of r. We remark that the most interesting aspect of the zero-temperature phase diagram is the presence of a range of p_0 values in which the minimal energy state is the hexatic one, a feature that to our knowledge has never been observed before. This hexatic phase could be possibly associated with the intermediate stage of the epithelial to mesenchymal transition, which occurs at similar values of p_0 [54].

IV. DISCUSSION

We rationalize the temperature dependence of the transition lines of the thermal phase diagram considering that p_0 affects

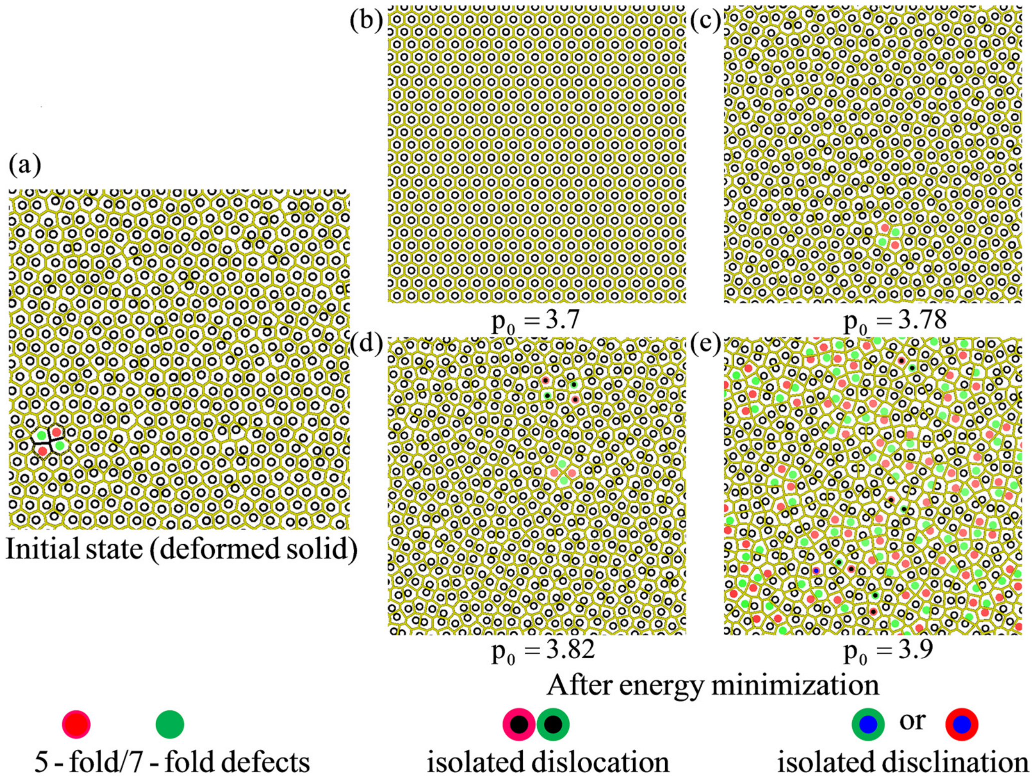

FIG. 6. The energy minimization process of a configuration in the deformed solid state (a) can end-up in configurations belonging to different phases, depending on the value of p_0. The hollow circles represent particles with six nearest neighbors, i.e., the hexagon-shaped cells. Red filled circles are fivefold defects and green filled circles are sevenfold defects. Isolated dislocations are marked by smaller black dots and isolated disclinations are illustrated with smaller blue dots. The snapshots illustrate only a small part of our investigated system.

the shear modulus of the particles, and hence that of the system. Indeed, as the single particle shear modulus [41], the macroscopic shear modulus decreases as p_0 increases, the two being roughly proportional [33]. Considering that according to the Lindemann criterion the melting transition occurs at a temperature $T_m \simeq \mu\lambda^2$, with λ a microscopic distance, e.g., a fraction of the interparticle separation, this explains the approximately linear dependence of the transition temperatures on p_0. We also note that, since in the affine approximation the single particle shear modulus is proportional to r^{-1}, the transition temperatures are expected to also scale as r^{-1}. Whereas the melted solid in the hexatic or the liquid phase depends on the free energy difference between these two phases, which is $\Delta f(p_0,T) = u_{\rm dis}(p_0) - T s_{\rm dis}$, where $u_{\rm dis}(p_0)$ is the energy required to unbind the dislocations, and $s_{\rm dis}$ is the corresponding entropy gain. $\Delta f(p_0,T_h) = 0$ identifies the limit of stability of the hexatic phase that occurs as long as $u_{\rm dis}(p_0) > T s_{\rm dis}$. As p_0 increases the hexatic phase becomes unstable as the unbinding energy decreases. In particular, since the range of p_0 values in which the hexatic phase is stable at zero temperature extends up to $p_0 = p_0^{\rm hl}$, we understand that $u_{\rm dis} < 0$ for $p_0 > p_0^{\rm hl}$. The entropic contribution to $\Delta f(p_0,T)$ drives the hexatic to liquid transition on increasing the temperature.

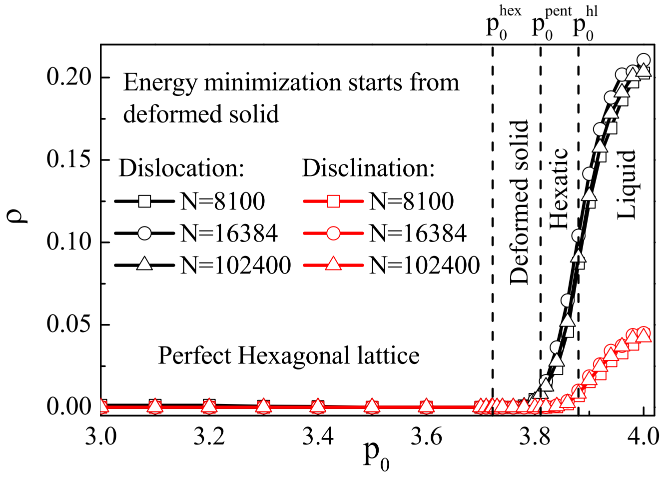

FIG. 7. p_0 dependence of the fraction of dislocations and disclinations of the zero-temperature states of the model with the smallest energy.

A qualitative understanding of the features of the zero temperature phase diagram is obtained considering that p_0 controls the degree of frustration of the system. Specifically, given that for the hexagonal crystal $p_0 = p_0^{\rm hex}$, $|p_0 - p_0^{\rm hex}|$ qualitatively acts as a degree of frustration of the hexagonal crystalline state, as also clear from Fig. 5. The increase of the degree of frustration of a system generally makes disordered the stable state. Accordingly, it is surprising that for $p_0 < p_0^{\rm hex}$ the hexagonal lattice remains the zero temperature phase, as if frustration was absent. Conversely, for $p_0 > p_0^{\rm hex}$ different phases are observed, as expected. We rationalize these observations considering that for $p_0 < p_0^{\rm hex}$, the hexagonal crystal

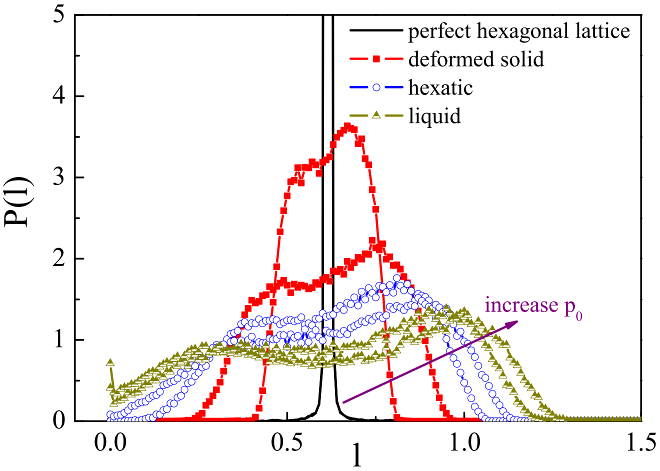

FIG. 8. p_0 dependence of the probability distribution of the lengths of the Voronoi edges of the zero-temperature states of the model with the smallest energy.

is frustrated as the particles should be more compact than the hexagons, a feature generally associated with polygons with many sides. However, since the system tessellates the space, states with an average number of sides per cell larger than six cannot exist because of Euler's theorem for planar graphs. We therefore understand that the model has a topological constraint that effectively prevents frustration to play its usual role for $p_0 < p_0^{\text{hex}}$. The same argument does not apply for $p_0 > p_0^{\text{hex}}$, where cells should be less compact than the hexagonal ones, and thus with an average number of sides smaller than six. Thus, for $p_0 > p_0^{\text{hex}}$ frustration plays its usual role. Indeed, the deformed solid region can be seen as a region of small frustration, which is not able to sensibly affect the zero temperature phase. Further increases of p_0, conversely, makes the zero temperature phase first of hexatic and then of liquid type. This scenario is consistent with the features of the distribution lengths of the Voronoi edges $P(l)$, illustrated in Fig. 8. In the crystalline phase, as expected, $P(l) = \delta(l - p_0^{\text{hex}}/6)$, regardless of the value of p_0. The distribution broadens and develops a bimodal shape in the deformed solid phase and in the hexatic one. Finally, in the liquid phase $P(l)$ develops a delta peak in zero, consistently with the emergence of a growing number of degenerate vertices.

Recent experimental studies have shown the existence of an intermediate phase in the epithelial to mesenchymal transition [37–39], which occurs at a measured value of p_0 consistent with those found in the Voronoi model [54]. This suggests that the observed intermediate phase could be of hexatic type. In this respect, it also worth noticing that a moderate polydispersity, which is expected to occur in actual tissues, does not affect the melting scenario [55]. We hope our results will stimulate relevant experimental work to test the nature of the intermediate epithelial-mesenchymal phase. Our results also suggests the possibility of using a Voronoi model with a different energy functional to investigate different systems of soft deformable particles at high density. Soft polymeric particles such as microgels, for instance, shrink and deform when compressed [56,57], which might help their crystallization [58]. In particular, neutral or large enough particles that do not undergo a counterion induced deswelling [58,59], might tessellate the space at large enough densities. This line of research might offer a novel approach to rationalize some unusual features of these systems, such as their high diffusivity [60] in a region of very high density, where particles are highly deformed. Finally, we remark that this model is shown to exhibit a hexatic phase at zero temperature in this work. Possibly, the investigation of the zero temperature melting transition could help rationalizing previous results that have found many parameters to affect the melting scenario in different systems [9–17,21,22].

ACKNOWLEDGMENTS

We acknowledge support from the Singapore Ministry of Education through the Academic Research Fund (Tier 2) *Many-Body Interactions In Concentrated Colloidal Suspensions* MOE2017-T2-1-066 (S), and are grateful to the National Supercomputing Centre (NSCC) of Singapore for providing computational resources. We thank R. Ni, D. Bi, and Y. Zheng for helpful discussions.

---

[1] J. G. Dash, Rev. Mod. Phys. **71**, 1737 (1999).
[2] U. Gasser, J. Phys.: Condens. Matter **21**, 203101 (2009).
[3] J. M. Kosterlitz and D. J. Thouless, J. Phys. C **6**, 1181 (1973).
[4] B. I. Halperin and D. R. Nelson, Phys. Rev. Lett. **41**, 121 (1978).
[5] A. P. Young, Phys. Rev. B **19**, 1855 (1979).
[6] S. T. Chui, Phys. Rev. B **28**, 178 (1983).
[7] Y. Saito, Phys. Rev. Lett. **48**, 1114 (1982).
[8] D. R. Nelson, Phys. Rev. B **18**, 2318 (1978).
[9] S. C. Kapfer and W. Krauth, Phys. Rev. Lett. **114**, 035702 (2015).
[10] D. E. Dudalov, E. N. Tsiok, Y. D. Fomin, and V. N. Ryzhov, J. Chem. Phys. **141**, 18C522 (2014).
[11] S. I. Lee and S. J. Lee, Phys. Rev. E **78**, 041504 (2008).
[12] M. Zu, J. Liu, H. Tong, and N. Xu, Phys. Rev. Lett. **117**, 085702 (2016).
[13] Y. Komatsu and H. Tanaka, Phys. Rev. X **5**, 031025 (2015).
[14] J. A. Anderson, J. Antonaglia, J. A. Millan, M. Engel, and S. C. Glotzer, Phys. Rev. X **7**, 021001 (2017).
[15] S. Deutschländer, T. Horn, H. Löwen, G. Maret, and P. Keim, Phys. Rev. Lett. **111**, 098301 (2013).
[16] W. Qi and M. Dijkstra, Soft Matter **11**, 2852 (2015).
[17] S. Prestipino, F. Saija, and P. V. Giaquinta, Phys. Rev. Lett. **106**, 235701 (2011).
[18] S. Deutschländer, A. M. Puertas, G. Maret, and P. Keim, Phys. Rev. Lett. **113**, 127801 (2014).
[19] W. Qi, A. P. Gantapara, and M. Dijkstra, Soft Matter **10**, 5449 (2014).
[20] K. Zahn, R. Lenke, and G. Maret, Phys. Rev. Lett. **82**, 2721 (1999).

[21] J. Russo and N. B. Wilding, Phys. Rev. Lett. **119**, 115702 (2017).

[22] E. P. Bernard and W. Krauth, Phys. Rev. Lett. **107**, 155704 (2011).

[23] A. L. Thorneywork, J. L. Abbott, D. G. A. L. Aarts, and R. P. A. Dullens, Phys. Rev. Lett. **118**, 158001 (2017).

[24] M. Watzlawek, C. N. Likos, and H. Löwen, Phys. Rev. Lett. **82**, 5289 (1999).

[25] C. von Ferber, A. Jusufi, C. N. Likos, H. Löwen, and M. Watzlawek, Eur. Phys. J. E **2**, 311 (2000).

[26] T. Terao, Mol. Phys. **104**, 2507 (2006).

[27] A. R. Denton, Phys. Rev. E **67**, 011804 (2003).

[28] N. L. Christos, H. Norman, J. Arben, and L. Hartmut, J. Phys.: Condens. Matter **15**, S233 (2003).

[29] N. Brodu, J. A. Dijksman, and R. P. Behringer, Phys. Rev. E **91**, 032201 (2015).

[30] R. Hohler and S. Cohen-Addad, Soft Matter **13**, 1371 (2017).

[31] R. Farhadifar, J.-C. Röper, B. Aigouy, S. Eaton, and F. Jülicher, Curr. Biol. **17**, 2095 (2007).

[32] D. B. Staple, R. Farhadifar, J.-C. Röper, B. Aigouy, S. Eaton, and F. Jülicher, Eur. Phys. J. E **33**, 117 (2010).

[33] D. Bi, J. H. Lopez, J. M. Schwarz, and M. L. Manning, Nat. Phys. **11**, 1074 (2015).

[34] M. L. Manning, R. A. Foty, M. S. Steinberg, and E.-M. Schoetz, Proc. Natl. Acad. Sci. U.S.A. **107**, 12517 (2010).

[35] A. G. Fletcher, M. Osterfield, R. E. Baker, and S. Y. Shvartsman, Biophys. J. **106**, 2291 (2014).

[36] R. C. Stone *et al.*, Cell Tissue Res. **365**, 495 (2016).

[37] N. V. Jordan, G. L. Johnson, and A. N. Abell, Cell Cycle **10**, 2865 (2011).

[38] H. Tanaka and S. Ogishima, J. Mol. Cell Biol. **7**, 253 (2015).

[39] R. Kalluri and R. A. Weinberg, J. Clin. Invest. **119**, 1420 (2009).

[40] D. Bi, X. Yang, M. C. Marchetti, and M. L. Manning, Phys. Rev. X **6**, 021011 (2016).

[41] See Supplemental Material at http://link.aps.org/supplemental/10.1103/PhysRevMaterials.2.045602 for additional information about the link of p_0 to the single cell elastic properties, the phase determination, and finite-size effects.

[42] M. Allen, *Computer Simulation of Liquids* (Oxford University Press, Oxford, 1987).

[43] M. Galassi *et al.*, *GNU Scientific Library Reference Manual* (Network Theory Ltd., United Kingdom, 2009), 3rd ed., http://www.gnu.org/software/gsl/.

[44] B. Schling, *The Boost C++ Libraries* (XML Press, Laguna Hills, CA, 2011).

[45] N. D. Mermin and H. Wagner, Phys. Rev. Lett. **17**, 1133 (1966).

[46] K. Bagchi, H. C. Andersen, and W. Swope, Phys. Rev. Lett. **76**, 255 (1996).

[47] C. Ruscher, J. Baschnagel, and J. Farago, Europhys. Lett. **112**, 66003 (2015).

[48] P. T. Kiss and A. Baranyai, J. Chem. Phys. **136**, 104109 (2012).

[49] E. de Miguel and G. Jackson, J. Chem. Phys. **125**, 164109 (2006).

[50] J. E. Mayer and W. W. Wood, J. Chem. Phys. **42**, 4268 (1965).

[51] M. Schrader, P. Virnau, and K. Binder, Phys. Rev. E **79**, 061104 (2009).

[52] C. N. Likos, A. Lang, M. Watzlawek, and H. Löwen, Phys. Rev. E **63**, 031206 (2001).

[53] D. M. Sussman and M. Merkel, arXiv:1708.03396.

[54] J.-A. Park *et al.*, Nat. Mater. **14**, 1040 (2015).

[55] S. Pronk and D. Frenkel, Phys. Rev. E **69**, 066123 (2004).

[56] D. Vlassopoulos and M. Cloitre, Curr. Opin. Colloid Interface Sci. **19**, 561 (2014).

[57] G. Romeo and M. P. Ciamarra, Soft Matter **9**, 5401 (2013).

[58] A. Scotti, U. Gasser, E. S. Herman, M. Pelaez-Fernandez, J. Han, A. Menzel, L. Lyon, and A. Fernández-Nieves, Proc. Natl. Acad. Sci. U.S.A. **113**, 5576 (2016).

[59] H. Kobayashi and R. G. Winkler, Sci. Rep. **6**, 19836 (2016).

[60] J. Mattsson, H. Wyss, A. Fernández-Nieves, K. Miyazaki, Z. Hu, D. Reichman, and D. A. Weitz, Nature (London) **462**, 83 (2009).